JPIChE 53(1) 2025: 31-45

Journal of the Pakistan Institute of Chemical Engineers

Journal homepage: www.piche.org.pk/journals

DOI: https://doi.org/10.54693/piche.05314

# Effect of Grit Blasting on Electrochemical Behavior of Anodized AZ31B Magnesium Alloy

F. Hussain[1]*, M.U. Manzoor[1], M. Kamran[1], T. Ahmad[1], F. Riaz[1], S. Mukhtar[1], W. Amin[1], B. Asghar[1]

*Submitted: 18/08/2024, Accepted: 22/07/2025, Published: 01/08/2025*

## Abstract

*Magnesium (Mg) alloys as biodegradable materials, are attracting significant importance for implant applications due to their suitability as biodegradable material. In the present research, An AZ31B Magnesium alloy was grit blasted with quartz and alumina particles with different blasting pressures and anodized in KOH solution for different durations to develop an anodized film on the different substrates. The surface morphology of the anodization layer was analyzed by scanning electron microscopy. The nature, coverage, and effectiveness of the anodized layer were investigated with potentiodynamic polarization (PD) scans and electrochemical impedance spectroscopy (EIS) in a simulated body fluid (SBF) solution. The results show an increase in surface coverage with an increase in anodization time. It is also revealed that a capacitive anodized layer with a dense inner layer having full coverage was obtained at 40 minutes anodization time for quartz and alumina blasted samples at 1000 kPa blasting pressure. The outcomes of this study help in developing a protective anodized film on the surface of Mg alloys for bone fixation implants.*

**Keywords:** AZ31B Magnesium Alloy, Grit Blasting, Blasting Pressure, Anodization, Potentiodynamic Polarization, Electrochemical Impedance Spectroscopy

## 1. Introduction:

Metallic biomaterials are currently extensively employed within the human body for implantation, such as in the form of artificial joints, stents, and bone plates. Permanent metallic implants may give rise to significant concerns due to their potential to induce adverse physiological responses and hinder the body's ability to adjust to growth and physiological changes [1-2]. Metal implants must be removed during a subsequent surgical procedure in these instances, however, this must be done after the tissue healing process is complete. Biodegradable implants offer a potential answer since they can be placed for the necessary duration to fix and then naturally dissolve, eliminating the risk of any negative reactions to the body [3-4]. Mg alloys have garnered growing interest in the past twenty years from both the industrial and academic sectors as a viable option for biodegradable biomedical devices, such as bone plates and vascular stents. This is primarily due to their unique characteristics, including a high strength-to-weight ratio, excellent electrical and thermal conductivities, shock absorption capabilities and exceptional vibration resistance [5-6]. Regarding materials commonly used, such as stainless steel, titanium alloys, and Cr-Co based alloys, it is worth noting that Mg and its alloys possess a relatively low density

---

[1] Institute of Metallurgy and Materials Engineering, University of the Punjab, Lahore
**Corresponding Author:** Faraz Hussain (faraz.imme@pu.edu.pk)

ranging from 1.74 to 2.0 g $cm^{-3}$. Additionally, they exhibit an elastic modulus ranging from 41 to 45 GPa. Furthermore, when these materials are implanted within the human body (in vivo), the ions and/or particles released as a result of corrosion phenomena do not cause any harm to the body [7]. However, the clinical application of Mg alloys has been restricted due to their inadequate resistance to corrosion. The degradation rate of Mg and its alloys is significantly high due to the highly negative reduction potential of Mg and its inadequate corrosion resistance in human body fluids or blood plasma. Consequently, the mechanical integrity of diseased or damaged bone tissue may not always be preserved during the healing process. High corrosion rates indicate high rates of hydrogen evolution, which in turn causes gas pockets to form around the implant and alkalization to occur near the corroding surface, both of which may be harmful to the local biological environment because water reduction is the common cathodic process during corrosion of Mg and its alloys [8].

The surface treatment of Mg is a widely employed method for mitigating corrosion [9-12]. Laser surface melting has the potential to enhance the corrosion resistance of Mg alloys by purifying the AZ91D β-phase and raising the aluminium concentration [13]. In addition to lowering the corrosion rate, heat treatment, which involves aging at elevated temperatures, can improve the surface microstructure of Mg [14]. In addition to surface treatment procedures, conversion coating, electroplating, and anodization are commonly employed methods [15]. However, when employed within the bio-environment, specific criteria must be met for the application of the coating. The coating must possess a substantial thickness, durability, and non-toxic nature. According to the current study, anodization has the highest probability of meeting these requirements when the electrolyte is properly formulated. Anodization treatment is an electrochemical procedure where a metal surface is transformed into an oxide coating with beneficial corrosion protection and functional characteristics [16]. It can improve the biocompatibility and adhesion of primers while increasing the wear resistance, hardness and film thickness compared to bare metal. The anodizing conditions significantly affect the characteristics of the anodized film.

Studies have examined the effects of electric parameters, electrolyte composition, and pre-and post-treatment on the characteristics of the anodized film [17-18]. However, the effect of surface roughness on the electrochemical behavior of anodized film on Mg alloys has not been published as far as we know. From this perspective, the main focus and aim of this research is to investigate the effect of surface roughness on the corrosion behavior of anodized film on Mg alloys in simulated body fluid (SBF).

## 2. Material and Methods:

### 2.1 Grit Blasting Process:

The AZ31B Mg alloy plate samples of 100 mm x 50 mm x 5 mm dimensions were selected as the substrate for the grit blasting procedure. The grit blasting procedure was conducted by using a special pressure blasting system. The system comprised an abrasive container, a blasting gun, a sample holder and an air compressor. Particles of abrasive material were drawn into the blasting gun and pushed through it by means of compressed air. An air pipe carried the compressed air from the compressor to the blasting gun. A nozzle angled at 90$^o$ to the sample surface directed the abrasive particles in the desired direction [19]. The grit blasting parameters that were selected for current study are abrasive type (alumina and quartz), abrasive size (<200 µm), blasting pressure (350, 700 and 1000 kPa), blasting angle (90$^o$), blasting distance (10 mm) and blasting time (20 sec).

### 2.2 Anodization Procedure:

The anodization procedure was conducted using a direct current power supply. Anodization was performed using an electrolyte with the composition listed in Table 1. Graphite served as the cathode and grit-blasted AZ31B Mg alloy samples served as the anode. The samples were anodized at room temperature for 10, 20, 30, and 40 minutes, using a constant voltage of 20V. Deionized water was used to rinse the anodized samples, and then they were dried in heated air [20].

**Table 1:** Composition of Electrolyte Solution

| Substance | $Na_3PO_4$ | KOH | KF | $Al(NO_3)_3$ | $Na_2SiO_3$ | Ethylene Glycol | Deionized Water |
|---|---|---|---|---|---|---|---|
| **Amount** | 8.197 g | 42.08 g | 0.15 g | 1.25 g | 0.075 g | 125 ml | 125 ml |

The process parameters applied to the samples were identified by labeling them according to the information provided in Table 2. The scanning electron microscopy (SEM, FEI Inspect S50) technique was employed to analyze the surface morphology of the anodized layer.

**Table 2:** Labelling of Samples

| Sample Labelling | Description |
|---|---|
| PS | Pristine Sample |
| A350, A700, A1000 | Alumina blasted samples at 350,700 and 1000 kPa |
| Q350, Q700, Q1000 | Quartz blasted samples at 350,700 and 1000 kPa |
| AT10, AT20, AT30, AT40 | Anodization time of 10, 20, 30 and 40 minutes |

### 2.3. Electrochemical Testing:

Potentiostat/Galvanostat/ZRA (Gamry Interface 1000E) was used to investigate the electrochemical behavior of anodized samples preblasted with quartz and alumina particles at different blasting pressures. The electrochemical investigations employed a three-electrode configuration with a working electrode (sample), reference electrode (Ag/AgCl saturated KCl), and counter electrode (graphite electrode). The exposed sample area was 1 cm$^2$. The electrolyte used was a Ringer's lactate solution which was kept at $37^{o}$C [21]. PD and EIS techniques were used to study the electrochemical behavior of anodized samples. The PD measurements were performed by applying a potential range of -0.5 to +1.5 V, with a scan rate of 5 mV/s. EIS was performed with an AC amplitude of ±10 mV(rms) with a test frequency ranging from $10^5$ to $10^{-2}$ Hz.

## 3. Results and Discussion:

### 3.1 Surface Morphology:

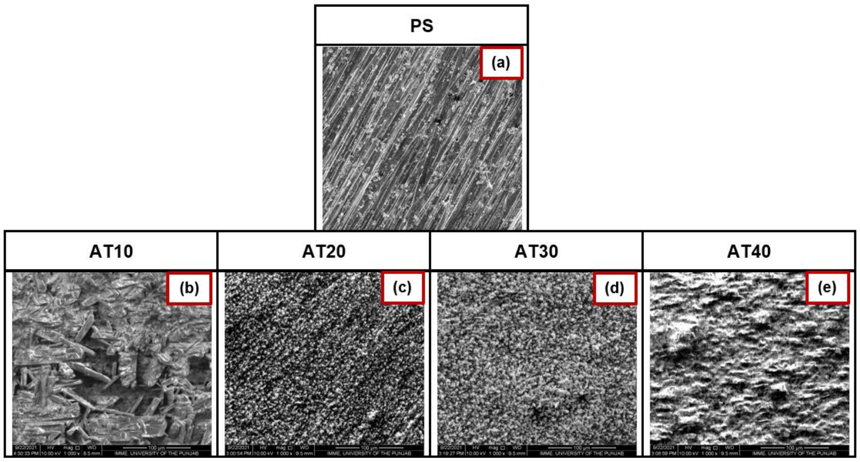

**Figure 1:** SEM Micrographs (Scale Bar: 300 µm) of Pristine Samples with Different Anodization Time

The SEM images of untreated and treated samples of pristine, quartz and alumina-blasted AZ31B Mg alloy are shown in Figs. 1-3, respectively. The SEM image of the untreated pristine sample, as depicted in Fig. 1(a), indicates the surface scratches resulting from the rolling process. A large flake-type anodizing layer with partial surface covering can be seen in Fig. 1(b) of the pristine sample after 10 minutes of anodizing treatment. However, coating morphology changes to a fine structure with full surface coverage when the anodizing time is increased from 10 to 20 minutes and coating morphology progressively becomes coarser as the anodizing treatment time increases, as seen in Figs. 1(c-e). The SEM images of quartz-blasted samples, subjected to a blasting pressure of 350 kPa, can be observed in Figs. 2(b-e). The surface morphology of these samples exhibits a similar pattern as observed in the anodized treated pristine samples. The samples subjected to quartz blasting at a pressure of 700 kPa are illustrated in Figs. 2(g-j). The 10 minutes anodizing treatment results in uniform coating which covers the entire sample. The anodized layer becomes coarser as the processing time increases to 40 minutes. The samples subjected to quartz blasting at a pressure of 1000 kPa, shown in Figs. 2(l-o), exhibit complete coverage during all anodizing times. The coating becomes increasingly coarse as the processing time increases.

The surface morphology of anodized samples blasted with alumina at various blasting shown in Fig. 3. It is evident that the coating coverage increases as the processing time increases. However, at 350 kPa blasting pressure, the relative coating coverage of alumina-blasted samples is lower, and at higher blasting pressures, it increases as the surface roughness increases. The change in morphology and surface coverage is due to the surface roughness of blasted samples [19]. The surface roughness of the alumina blasted samples is higher than that of the pristine sample and quartz blasted samples. The nature of crest and trough provided a reaction site for the development of anodized products. The high energy surface layer of quartz and alumina blasted samples help to increase the interaction of magnesium with solution to form anodized layer. Anodization of magnesium is a complex process, the anodized layer formed on the surface acts as barrier and prevents further oxidation [22-23].

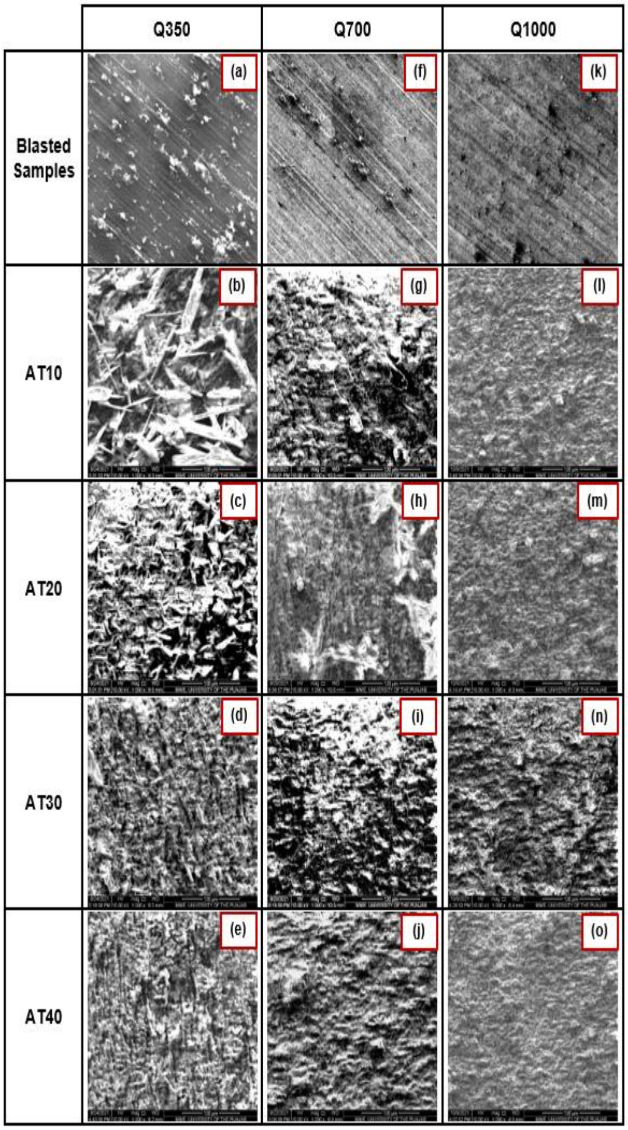

**Figure 2:** SEM Micrographs (Scale Bar: 300 µm) of Quartz Blasted Samples with Different Anodization

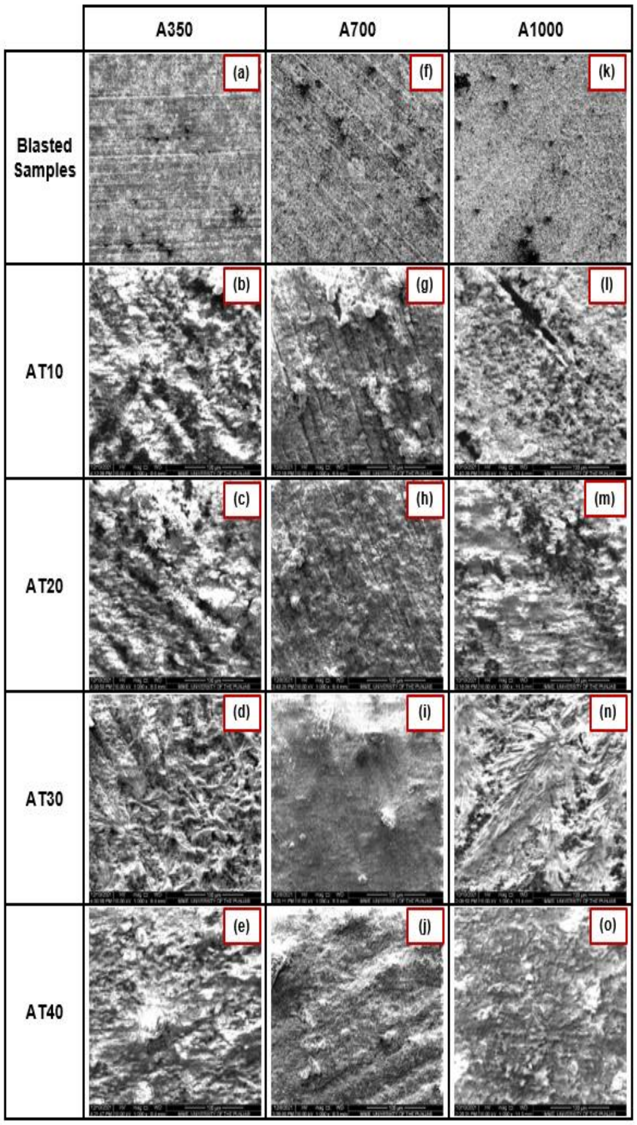

**Figure 3:** SEM Micrographs (Scale Bar: 300 µm) of Alumina Blasted Samples with Different Anodization Time

### 3.2. Potentiodynamic Polarization Scan:

The potentiodynamic polarization curves of pristine samples anodized for different time periods in SBF solution are shown in Fig. 4. Similarly, the polarization curves of samples, blasted with quartz and alumina particles at different blasting pressures, anodized for different time periods in SBF solution are shown in Figs. 5 – 10. The corrosion current density ($I_{corr}$), corrosion potential ($E_{corr}$), and corrosion rate values were determined from the tafel scans using tafel extrapolation incorporating the linear portion using Gamry EChem Analyst software. Similarly, the polarization resistance ($R_p$) was calculated by the formula as given in Eq. 1 [24]:

$$R_p = \frac{\beta_a\beta_c}{2.303 I_{corr}(\beta_a+\beta_c)} \quad (1)$$

where βa and βc are the anodic and cathodic Tafel slopes.

The measured values of $I_{corr}$, $E_{corr}$, corrosion rate and $R_p$ are listed in Tables 3 – 5. In a potentiodynamic scan, the anodic polarization curve indicates the behavior of metal dissolution as given in Eq. 2

$$Mg = Mg^{2+} + 2e^- \text{ or } Mg_{(s)} + 2(OH)^- = Mg(OH)_{2(s)} + 2e^- \quad (2)$$

while cathodic polarization curve reveals evolution of hydrogen as given in Eq. 3 [25].

$$2H_2O + 2e^- = 2(OH)^- + H_2 \text{ or } 2H^+ + 2e^- = H_{2(g)} \quad (3)$$

Good corrosion resistance can be indicated by more positive $E_{corr}$, lower $I_{corr}$ and high $R_p$ [26]. The cathodic polarization curves of pristine anodized samples show a linear trend over the whole polarization range. On the contrary, anodic polarization curves of pristine anodized samples show a gradual increase in the tendency towards passivation behavior as depicted in Fig. 4. From the data given in Table 3, a major shift of $E_{corr}$ values towards positive potential, tremendous decreases in $I_{corr}$ values and corrosion rates and enormous increases in $R_p$ values can be observed with increase in anodization time. The values of corrosion rates show about 29-fold decrease in corrosion rate with an increase in anodization time, which demonstrates the coating effectiveness. The values of $R_p$ show about 136-fold increase in polarization resistance, confirming the resistance behavior of the coating

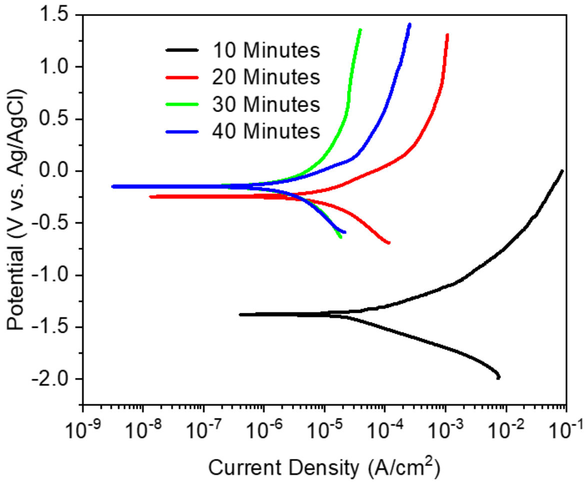

**Figure 4:** PD Curves of Pristine Samples with Different Anodization Time in SBF

.

**Table 3:** Electrochemical Parameters of Pristine Samples with Different Anodization Time

| Sample | Electrochemical Parameters | | | |
|---|---|---|---|---|
| | $E_{corr}$ (mV) | $I_{corr}$ (μA/cm²) | Corrosion Rate (mpy) | $R_p$ (KΩcm²) |
| PS-AT10 | -1408.9 | 26.718 | 48.138 | 1.48 |
| PS-AT20 | -247.1 | 6.407 | 11.54 | 8.61 |
| PS-AT30 | -143.3 | 0.987 | 3.097 | 56.12 |
| PS-AT40 | -149.8 | 0.325 | 1.657 | 202.28 |

The cathodic and anodic polarization curves of Q350-AT10 – Q350-AT40 samples, as shown in Fig. 5(a), show a similar trend as that of pristine samples. It can be observed from the data presented in Table 4 that $E_{corr}$, $I_{corr}$ and corrosion rates decrease enormously, and $R_p$ increases tremendously with an increase in anodization time. The near zero value of $I_{corr}$ confirms the complete coverage in Q350-AT40 sample (0.035 μA/cm²) compared to Q350-AT10 sample (21.271 μA/cm²). Table 4 show 287-fold decrease in corrosion rate with increase in anodization time which clearly indicates the effectiveness of the anodized film. The values of $R_p$ of these samples show 1057-fold increase in polarization resistance, confirming the resistance behavior of the anodized film. The cathodic and anodic polarization curves of Q700-AT10 – Q700-AT40 samples are represented in Fig. 5(b). By analyzing the data shown in Table 4, it is evident that $I_{corr}$ and corrosion rates decreases, and $R_p$ increases with an increase in the anodization period. The near-to-zero value of $I_{corr}$ confirms the complete coverage in Q700-AT40 sample (0.028 μA/cm²) compared to Q700-AT10 sample (15 μA/cm²). Likewise, the corrosion rates of these samples exhibit a significant reduction of 359-fold, which clearly proves the efficiency of the anodized layer. The $R_p$ values of the samples demonstrate a 1086-fold increase in polarization resistance, which confirms the resistance characteristics of the anodized layer. The cathodic and anodic polarization curves of Q1000-AT10 – Q1000-AT40 samples are illustrated in Fig. 5(c). It is evident from the data presented in Table 4 that the $I_{corr}$ and corrosion rates decreases, and $R_p$ increases with an increase in the anodization duration. The near zero value of $I_{corr}$ indicates that Q1000-AT40 sample (0.019 μA/cm$^2$) has achieved full coverage compared to Q1000-AT10 sample (10.654 μA/cm$^2$). Similarly, the values of corrosion rates show a 281-fold decrease in corrosion rate, demonstrating the coating becomes more effective. Similarly, the $R_p$ values show an 809-fold increase in polarization resistance, confirming the resistive behavior of the coating [27-29].

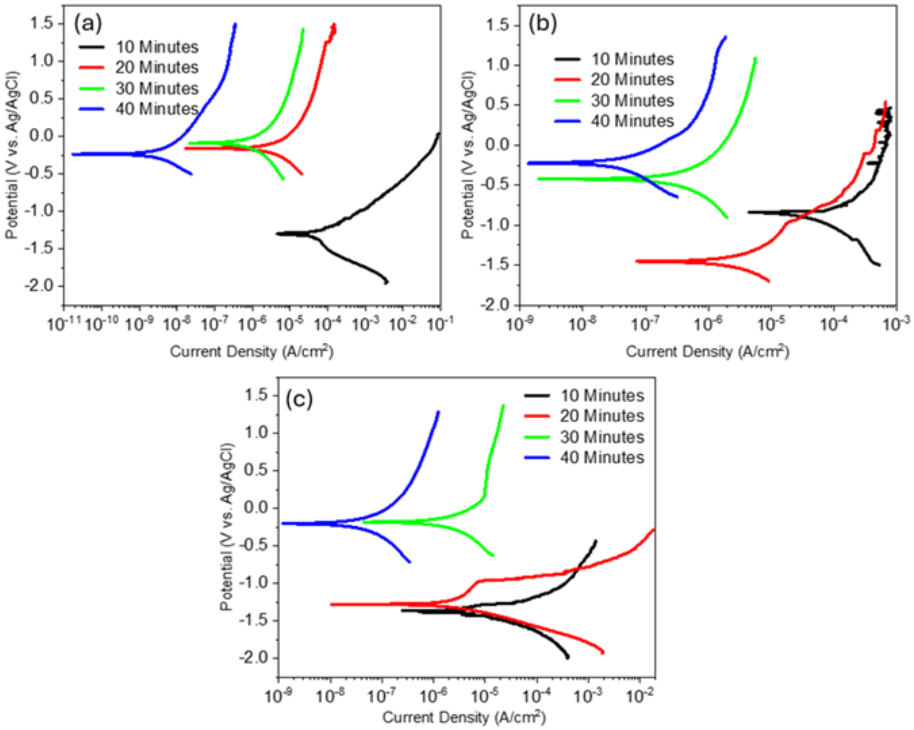

**Figure 5:** PD curves with different anodization times in SBF for quartz blasted samples at a blasting pressure of (a) 350 kPa (b) 700 kPa (c) 1000 kPa.

**Table 4:** Electrochemical Parameters of Quartz Blasted Samples with Different Anodization Time

| **Sample** | **Electrochemical Parameters** | | | |
|---|---|---|---|---|
| | **$E_{corr}$ (mV)** | **$I_{corr}$ (μA/cm$^2$)** | **Corrosion Rate (mpy)** | **$R_p$ (KΩcm$^2$)** |
| Q350-AT10 | -1299.1 | 21.271 | 39.4 | 1.61 |
| Q350-AT20 | -160.7 | 2.340 | 4.2 | 27.69 |
| Q350-AT30 | -85.3 | 0.590 | 1.06 | 112.77 |
| Q350-AT40 | -239.4 | 0.035 | 0.137 | 1702.41 |
| Q700-AT10 | -851.1 | 15.000 | 31.3 | 2.19 |
| Q700-AT20 | -1460.6 | 1.730 | 3.12 | 37.56 |
| Q700-AT30 | -423.3 | 0.445 | 0.802 | 146.83 |
| Q700-AT40 | -226.1 | 0.028 | 0.087 | 2379.42 |
| Q1000-AT10 | -1395.9 | 10.654 | 13.8 | 4.22 |
| Q1000-AT20 | -1256.8 | 1.413 | 2.906 | 47.67 |
| Q1000-AT30 | -181.2 | 0.279 | 0.323 | 237.93 |
| Q1000-AT40 | -206.1 | 0.019 | 0.049 | 3416.92 |

The anodized samples (A350-AT10 – A350-AT40) exhibit cathodic and anodic polarization curves that have a similar pattern to the pristine samples are shown in Fig. 6(a). It can be observed from the data presented in Table 5 that $I_{corr}$ and corrosion rates decreases, and $R_p$ increases with an increase in the anodization time. The near-to-zero value of $I_{corr}$ (0.025 μA/cm$^2$) confirms the full coverage in A350-AT40 sample compared to A350-AT10 sample (2.969 μA/cm$^2$). Similarly, the $R_p$ values show a 121-fold increase in polarization resistance, confirming the resistance behavior of the barrier film. Likewise, the values of corrosion rates show a 35-fold decrease in corrosion rate, which proves the efficiency of the barrier film. The anodized samples (A700-AT10 – A700-AT40) exhibit cathodic and anodic polarization curves are shown in Fig. 6(b). By analyzing the data shown in Table 5, it is evident that $I_{corr}$ and corrosion rates decreases, and $R_p$ increases with an increase in the anodization duration. The almost zero value of $I_{corr}$ (0.018 μA/cm$^2$) indicates that A700-AT40 sample has achieved full coverage compared to A700-AT10 sample (2.211 μA/cm$^2$). Likewise, the corrosion rates values show a 300-fold decrease in corrosion rate, demonstrating the coating effectiveness. Likewise, the $R_p$ values show a 132-fold increase in polarization resistance, confirming the resistance characteristic of the barrier layer. The anodized samples (A1000-AT10 – A1000-AT40) exhibit cathodic and anodic polarization curves are illustrated in Fig. 6(c). From the data given in Table 5, it can be observed that the $I_{corr}$ and corrosion rates decreases, and $R_p$ increases with an increase in the anodization period. The nearly zero value of $I_{corr}$ indicates that A1000-AT40 sample has achieved full coverage (0.008 μA/cm$^2$) compared to A1000-AT10 sample (2.033 μA/cm$^2$). Likewise, the corrosion rates exhibit a significant reduction of 434-fold, which clearly proves the efficiency of the barrier film. Similarly, the $R_p$ values demonstrate a 149-fold increase in polarization resistance, which confirms the resistance characteristics of the barrier film [27-29]. The results of PD scans revealed that the lower corrosion current density and high polarization resistance of anodized samples blasted with alumina suggest that a protective anodized film developed on alumina-blasted samples may be suitable for bone fixation implants [30].

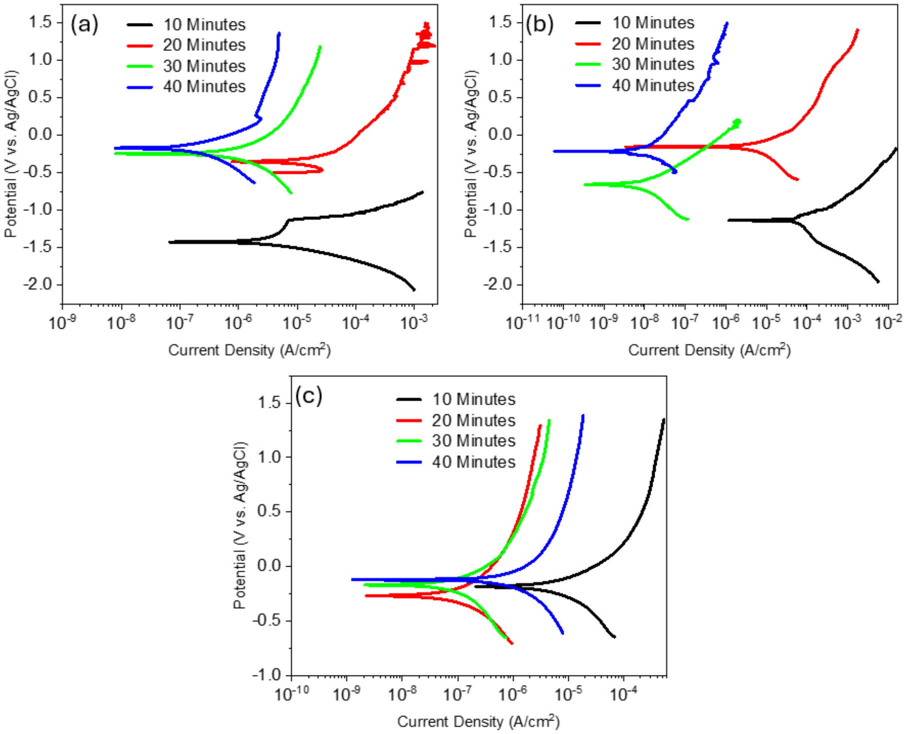

**Figure 6:** PD curves with different anodization times in SBF for alumina blasted samples at a blasting pressure of (a) 350 kPa (b) 700 kPa (c) 1000 kPa.

**Table 5:** Electrochemical Parameters of Alumina Blasted Samples with Different Anodization Time

| Sample | Electrochemical Parameters | | | |
|---|---|---|---|---|
| | $E_{corr}$ (mV) | $I_{corr}$ (μA/cm$^2$) | Corrosion Rate (mpy) | $R_p$ (KΩcm$^2$) |
| A350-AT10 | -1418.8 | 2.969 | 5.35 | 18.26 |
| A350-AT20 | -353.4 | 1.399 | 2.52 | 47.48 |
| A350-AT30 | -238.7 | 0.521 | 0.982 | 119.90 |
| A350-AT40 | 157.7 | 0.025 | 0.125 | 2212.55 |
| A700-AT10 | -1141.3 | 2.211 | 4.21 | 29.51 |
| A700-AT20 | -134.9 | 0.912 | 1.92 | 56.69 |
| A700-AT30 | -653.1 | 0.201 | 0.504 | 318.45 |
| A700-AT40 | -215.9 | 0.018 | 0.014 | 3907.62 |
| A1000-AT10 | -176.2 | 2.033 | 3.91 | 35.75 |

| | | | | |
|---|---|---|---|---|
| A1000-AT20 | -265.4 | 0.775 | 0.124 | 80.35 |
| A1000-AT30 | -169.4 | 0.114 | 0.221 | 550.08 |
| A1000-AT40 | -121.6 | 0.008 | 0.009 | 5349.91 |

### 3.3 Electrochemical Impedance Spectroscopy:

The EIS results in the form of Nyquist plot and corresponding Bode plots are helpful in understanding the nature of the anodized film developed on the surface. Depressed semicircle at the intermediate frequencies in Nyquist plot is a characteristic of capacitive behavior shown by an anodic film/layer and the diameter of the particular capacitive loop shows the degree of charged transfer resistance during corrosion/electrochemical reactions at the electrode surface across the film/coating in the test solution. The larger the diameter of the capacitive semicircle and higher the impedance value (Z” value), the greater the corrosion resistance [31]. A higher impedance value in the lower frequency range in Bode-impedance plot indicates higher corrosion resistance [32-33]. An equivalent electrical circuit (EEC) can be fitted on the experimental EIS data to determine the quantitative values such as solution resistance ($R_s$), surface oxide film resistance ($R_f$), charge transfer resistance ($R_{ct}$) and constant phase elements (CPEs). Constant phase elements (CPEs) such as capacitance of surface oxide film ($CPE_f$) and capacitance of double layer ($CPE_{dl}$) are usually preferred instead of pure capacitance to incorporate heterogeneity of the electrode surface [34]. The impedance of a CPE ($Z_{CPE}$) can be calculated by the formula as shown in Eq. 4 [35]:

$$Z_{CPE} = [Q(j\omega)^n]^{-1} \qquad (4)$$

where j = complex operator, $\omega$ = angular frequency, Q = magnitude of the CPE (related to its capacitance), n = exponent of the CPE [n=1 for an ideal capacitor, n=0.5 for diffusion-controlled electrodes, n=0 for an ideal resistor, intermediate values of n (0<n<1) are obtained for actual electrodes].

The EEC, shown in Fig. 7, was used to fit on the EIS data of the anodized samples. The fitted values of the circuit parameters are listed in Tables 6 – 8.

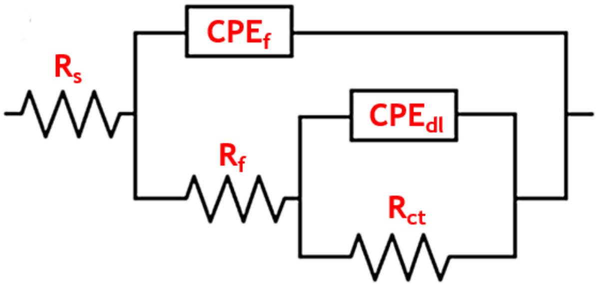

**Figure 7:** Equivalent Electrical Circuit (EEC) Model

The EIS results of pristine samples anodized for 10 to 40 minutes in SBF solution are shown in Fig. 8. The Nyquist plots [Fig. 8(a)] clearly shows the capacitive behavior for all the coatings developed on all the samples. However, the highest Z” value i.e. 1027.2 $\Omega.cm^2$ and the large diameter of the depressed semicircles along the Z’ axis for 40 minutes of anodizing time confirms the formation of anodized film with higher capacitance. Similarly, the Bode-impedance modulus plot [Fig. 8(b)] shows the maximum value of 8205.3 $\Omega.cm^2$ at a lower frequency for PS-AT40 compared to others samples confirming the maximum corrosion resistance for this sample. The fitted values of the circuit parameters for pristine anodized samples are shown in Table 6. The higher values of $R_f$ (8.4 $k\Omega.cm^2$) and $R_{ct}$ (23.1 $k\Omega.cm^2$) for PS-AT40 sample as compared to other anodized samples confirms the protection nature of the anodized layer. The higher values of $R_{ct}$ than that of $R_f$ for all anodizing times confirm the formation of dense layer at the interface beneath the outer porous layer. Similarly, the decreasing trend of both $CPE_{dl}$ and $CPE_f$ with increasing anodizing time confirms the increase in compactness and pore free anodized film due to a decrease in the effective area exposed to the electrolyte [36].

**Table 6:** Circuit Parameters of Pristine Samples with Different Anodization Time

| **Sample** | **Circuit Parameters** | | | | |
|---|---|---|---|---|---|
| | **$R_s$ ($\Omega.cm^2$)** | **$R_f$ ($k\Omega.cm^2$)** | **$CPE_f$ ($S.s^n.cm^{-2}$)** | **$R_{ct}$ ($k\Omega.cm^2$)** | **$CPE_{dl}$ ($S.s^n.cm^{-2}$)** |
| PS-AT10 | 41.2 | 4.3 | 7.46E-6 | 10.2 | 9.78E-4 |

| | | | | | |
|---|---|---|---|---|---|
| PS-AT20 | 43.8 | 5.1 | 6.67E-6 | 14.3 | 8.89E-4 |
| PS-AT30 | 40.3 | 6.8 | 5.71E-6 | 17.9 | 6.92E-4 |
| PS-AT40 | 46.8 | 8.4 | 4.98E-6 | 23.1 | 5.10E-4 |

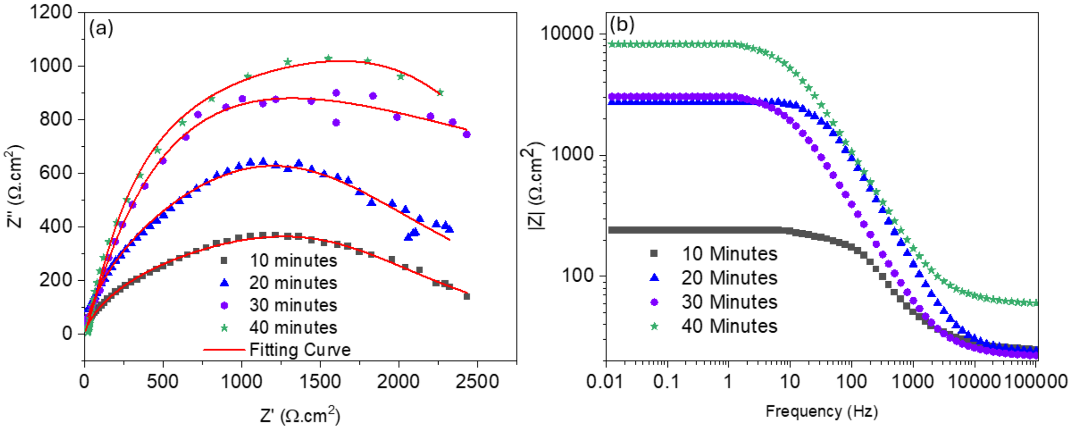

**Figure 8:** EIS of Pristine Samples with Different Anodization Time in SBF (a) Nyquist Plot (b) Bode-Impedance Modulus Plot

The EIS outcomes of anodized samples (Q350-AT10 – Q350-AT40) in SBF solution are illustrated in Fig. 9. The capacitive behavior of all the anodized samples is evident from the impedance values obtained from the Nyquist plot [Fig. 9(a)]. However, the Z” value (1284 Ω.cm$^2$) and the relatively larger diameter of the depressed semicircles along the Z’ axis confirm that the Q350-AT40 sample has higher corrosion resistance compared to the other processed samples. Likewise, the Bode-impedance modulus plot [Fig. 9(b)] indicates a maximum value of 9351 Ω.cm$^2$ at a lower frequency for Q350-AT40 sample as compared to other samples which confirms its maximum corrosion resistance. The fitted values of the circuit parameters for Q350-AT10 – Q350-AT40 samples are displayed in Table 7. The higher values of $R_f$ (10.9 kΩ.cm$^2$) and $R_{ct}$ (27.2 kΩ.cm$^2$) for Q350-AT40 sample compared to other anodized samples confirms the protective nature of the anodized film. Likewise, as the anodizing duration increases, $CPE_{dl}$ and $CPE_f$ tend to decrease, which means that the less electrode surface is exposed to electrolyte due to compact and pore-free anodized film [36]. The EIS findings of anodized samples (Q700-AT10 – Q700-AT40) in SBF solution are displayed in Fig. 10. All the anodized samples exhibit capacitive behavior, as seen by the impedance values from the Nyquist plot [Fig. 10(a)]. The Z” value (3486 Ω.cm$^2$) and the diameter of the depressed semicircles along the Z’ axis demonstrate that the Q700-AT40 sample has a higher corrosion resistance compared to the other treated samples. Likewise, the Bode-impedance modulus plot [Fig. 10(b)] shows the value 16540 Ω.cm$^2$ at lower frequency for Q700-AT40 sample confirming the maximum corrosion resistance. The circuit parameter fitted values for Q700-AT10 – Q700-AT40 samples are presented in Table 7. $R_f$ (13.4 kΩ.cm$^2$) and $R_{ct}$ (30.2 kΩ.cm$^2$), which are the highest for the Q700-AT40 sample than that of other anodized samples, prove that the anodized layer is protective. Similarly, decrease in $CPE_{dl}$ and $CPE_f$ with increase in anodizing time is other evidence that the anodized layer is compact and pore-free inner layer and porous outer layer with reduced effective area exposed to the electrolyte. The EIS studies of anodized samples (Q1000-AT10 – Q1000-AT40) in SBF solution are shown in Fig. 11. The Nyquist plot [Fig. 11(a)] clearly indicates the capacitive nature of all the anodized samples based on the impedance values. In contrast to the other treated samples, the Q1000-AT40 sample demonstrated maximum corrosion resistance, as confirmed by the highest Z" value of 8553 Ω.cm$^2$ and the maximum diameter of the depressed semicircles along the Z' axis. Likewise, the highest corrosion resistance for the Q1000-AT40 sample is confirmed by the Bode-impedance modulus plot, shown in Fig. 11(b), with the highest value of 38063 Ω.cm$^2$ at lower frequencies. The circuit parameter fitted values for Q1000-AT10 – Q1000-AT40 samples are provided in Table 7. The highest values of $R_f$ (15.8 kΩ.cm$^2$) and $R_{ct}$ (33.5 kΩ.cm$^2$) for the Q1000-AT40 sample, in comparison to other anodized samples, confirming the protective characteristics of the barrier layer. The observed decline in both $CPE_{dl}$ and $CPE_f$ as anodizing time increases provides further evidence of the compactness and pore-free barrier film resulting from a reduced surface area exposed to the electrolyte.

**Table 7:** Circuit Parameters of Quartz Blasted Samples with Different Anodization Time

| **Sample** | **Circuit Parameters** | | | | |
|---|---|---|---|---|---|
| | **$R_s$ ($\Omega.cm^2$)** | **$R_f$ ($k\Omega.cm^2$)** | **$CPE_f$ ($S.s^n.cm^{-2}$)** | **$R_{ct}$ ($k\Omega.cm^2$)** | **$CPE_{dl}$ ($S.s^n.cm^{-2}$)** |
| Q350-AT10 | 42.2 | 5.4 | 7.25E-6 | 11.3 | 9.22E-4 |
| Q350-AT20 | 44.9 | 7.6 | 6.34E-6 | 17.4 | 8.65E-4 |
| Q350-AT30 | 46.6 | 9.7 | 5.16E-6 | 21.5 | 6.31E-4 |
| Q350-AT40 | 48.3 | 10.9 | 4.67E-6 | 27.2 | 4.32E-4 |
| Q700-AT10 | 43.2 | 6.6 | 7.05E-6 | 13.5 | 8.65E-4 |
| Q700-AT20 | 47.1 | 8.5 | 6.21E-6 | 19.2 | 6.51E-4 |
| Q700-AT30 | 49.8 | 10.3 | 4.32E-6 | 25.4 | 5.23E-4 |
| Q700-AT40 | 51.2 | 13.4 | 3.58E-6 | 30.2 | 4.42E-4 |
| Q1000-AT10 | 39.4 | 7.1 | 6.67E-6 | 15.7 | 6.56E-4 |
| Q1000-AT20 | 41.7 | 9.3 | 5.32E-6 | 21.2 | 4.45E-4 |
| Q1000-AT30 | 48.2 | 11.7 | 3.31E-6 | 28.3 | 3.24E-4 |
| Q1000-AT40 | 52.5 | 15.8 | 2.14E-6 | 33.5 | 2.43E-4 |

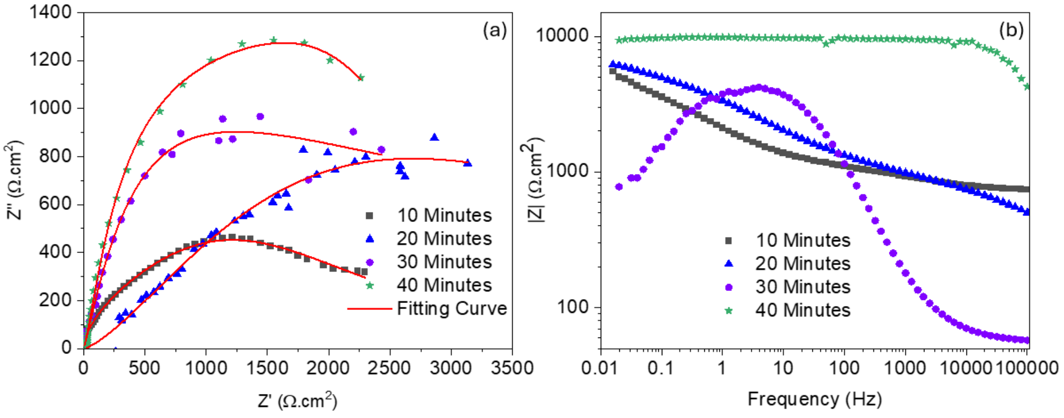

**Figure 9:** EIS of Quartz Blasted Samples at 350 kPa Blasting Pressure with Different Anodization Time in SBF (a) Nyquist Plot (b) Bode-Impedance Modulus Plot

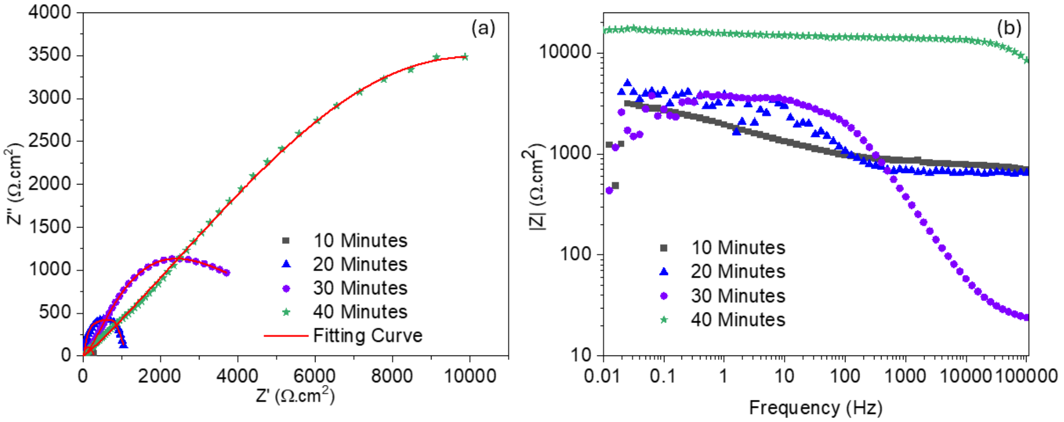

**Figure 10:** EIS of Quartz Blasted Samples at 700 kPa Blasting Pressure with Different Anodization Time in SBF (a) Nyquist Plot (b) Bode-Impedance Modulus Plot

The EIS outcomes of anodized samples (A350-AT10 – A350-AT40) in SBF solution are illustrated in Fig. 12. The capacitive behavior of all the anodized samples is evident from the impedance values obtained from the Nyquist plot [Fig. 12(a)]. However, the highest Z" value, which is 159820 Ω.cm$^2$, and the maximum diameter of the depressed semicircles along the Z' axis confirm that the A350-AT40 sample has higher corrosion resistance compared to the other processed samples. Likewise, the Bode-impedance modulus plot [Fig. 12(b)] indicates a maximum value of 836000 Ω.cm² at lower frequency for A350-AT40 sample which confirms its maximum corrosion resistance.

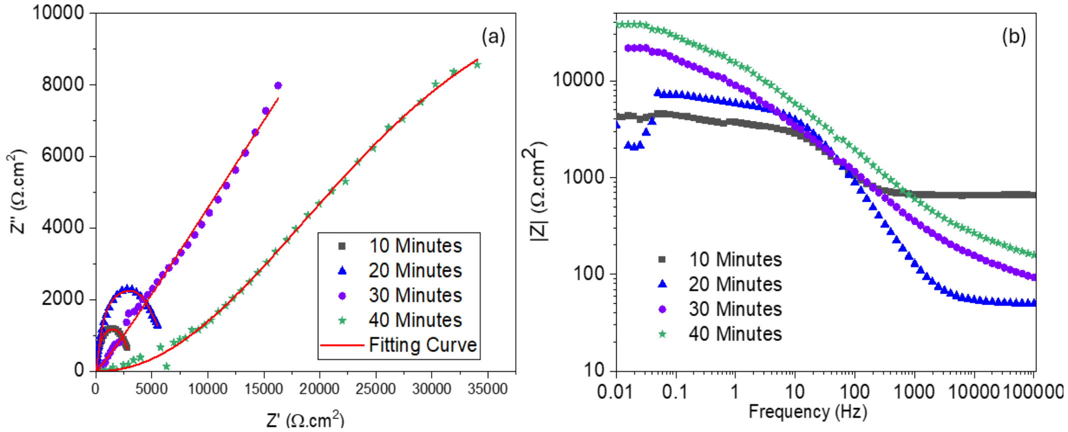

**Figure 11:** EIS of Quartz Blasted Samples at 1000 kPa Blasting Pressure with Different Anodization Time in SBF (a) Nyquist Plot (b) Bode-Impedance Modulus Plot

The fitted values of the circuit parameters for A350-AT10 – A350-AT40 are displayed in Table 8. The highest values of $R_f$ (31.4 kΩ.cm²) and $R_{ct}$ (51.2 kΩ.cm²) for A350-AT40 sample compared to other anodized samples confirms the protective nature of the anodized film. As the anodizing duration increases, $CPE_{dl}$ and $CPE_f$ tend to decrease, which means that the electrolyte is exposed to less of the film, leading to a more compact and pore-free anodized film. The EIS results of anodized samples (A700-AT10 – A700-AT40) in SBF solution are displayed in Fig. 13. All the anodized samples exhibit capacitive behavior, as seen by the impedance values from the Nyquist plot [Fig. 13(a)]. The Z" value, which is 249000 Ω.cm², and the diameter of the depressed semicircles along the Z' axis demonstrate that theA700-AT40 sample has a higher corrosion resistance compared to the other treated samples. Likewise, the Bode-impedance modulus plot [Fig. 13(b)] shows the value 4066000 Ω.cm² at lower frequency for A700-AT40 sample confirming the maximum corrosion resistance. The circuit parameter fitted values for A700-AT10 – A700-AT40 samples are presented in Table 8. $R_f$ (39.9 kΩ.cm²) and $R_{ct}$ (59.5 kΩ.cm²), which are the highest for the A700-AT40 sample than that of other anodized samples, prove that the anodized layer is protective. The fact that $CPE_{dl}$ and $CPE_f$ tend to decrease as the anodizing time increases is another evidence that the anodized layer is compact and pore-free due to the reduced effective area exposed to the electrolyte. The EIS outcomes of anodized samples (A1000-AT10 – A1000-AT40) in SBF solution are depicted in Fig. 14. The Nyquist plot [Fig. 14(a)] clearly indicates the capacitive nature of all the anodized samples based on the impedance values. In contrast to the other treated samples, the A1000-AT40 sample demonstrated maximum corrosion resistance, as confirmed by the highest Z" value of 336700 Ω.cm² and the maximum diameter of the depressed semicircles along the Z' axis.

**Table 8:** Circuit Parameters of Alumina Blasted Samples with Different Anodization Time

| Sample | Circuit Parameters | | | | |
|---|---|---|---|---|---|
| | $R_s$ (Ω.cm²) | $R_f$ (kΩ.cm²) | $CPE_f$ (S.sⁿ.cm⁻²) | $R_{ct}$ (kΩ.cm²) | $CPE_{dl}$ (S.sⁿ.cm⁻²) |
| A350-AT10 | 40.2 | 21.3 | 8.15E-7 | 41.6 | 10.98E-3 |
| A350-AT20 | 36.4 | 24.6 | 7.43E-7 | 45.4 | 9.87E-3 |
| A350-AT30 | 38.2 | 27.7 | 6.21E-7 | 48.2 | 8.89E-3 |
| A350-AT40 | 41.3 | 31.4 | 5.87E-7 | 51.2 | 7.78E-3 |
| A700-AT10 | 45.2 | 27.3 | 7.98E-7 | 45.9 | 9.87E-3 |
| A700-AT20 | 37.3 | 30.2 | 6.76E-7 | 51.5 | 8.87E-3 |

| | | | | | |
|---|---|---|---|---|---|
| A700-AT30 | 43.4 | 33.3 | 5.22E-7 | 54.6 | 7.65E-3 |
| A700-AT40 | 48.3 | 39.9 | 4.14E-7 | 59.5 | 6.71E-3 |
| A1000-AT10 | 35.4 | 34.3 | 7.10E-7 | 53.2 | 9.10E-3 |
| A1000-AT20 | 31.2 | 39.7 | 6.21E-7 | 59.8 | 8.89E-3 |
| A1000-AT30 | 30.6 | 41.4 | 4.87E-7 | 63.2 | 6.53E-3 |
| A1000-AT40 | 39.8 | 45.5 | 3.65E-7 | 67.4 | 4.32E-3 |

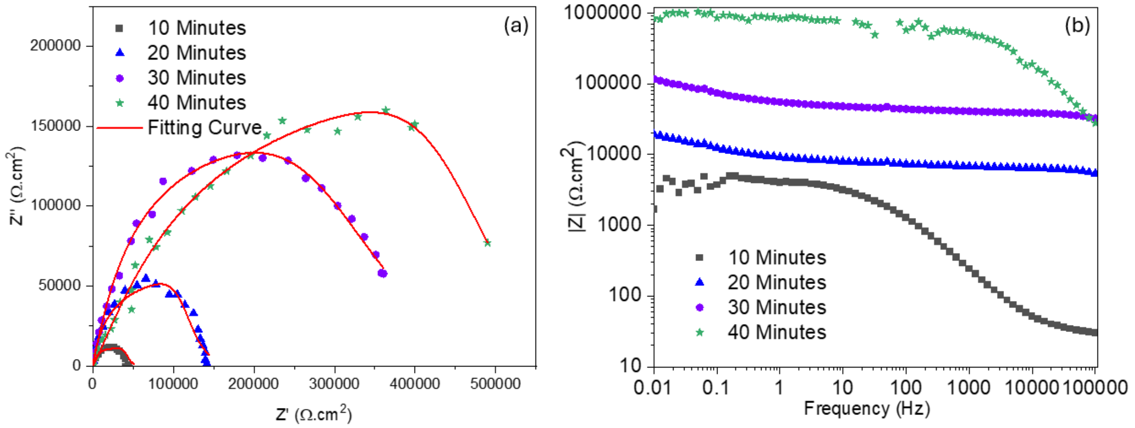

**Figure 12:** EIS of Alumina Blasted Samples at 350 kPa Blasting Pressure with Different Anodization Time in SBF (a) Nyquist Plot (b) Bode-Impedance Modulus Plot

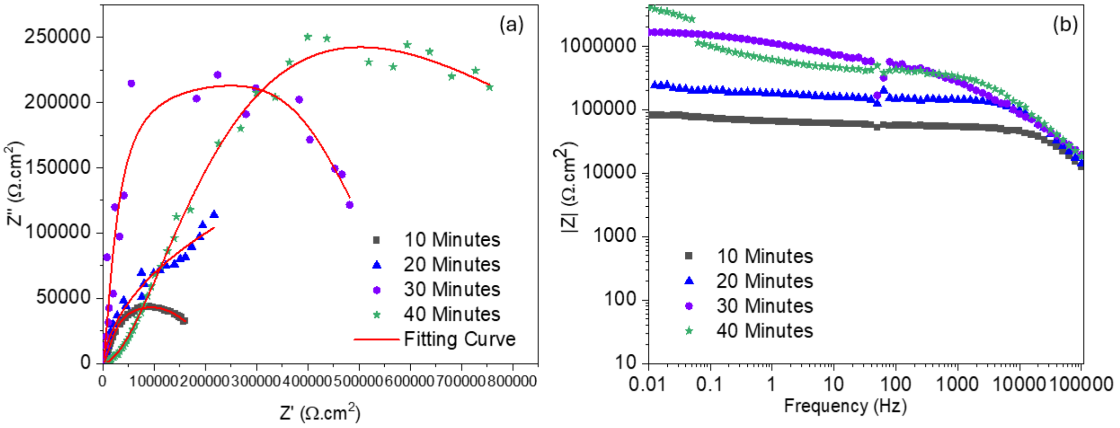

**Figure 13:** EIS of Alumina Blasted Samples at 700 kPa Blasting Pressure with Different Anodization Time in SBF (a) Nyquist Plot (b) Bode-Impedance Modulus Plot

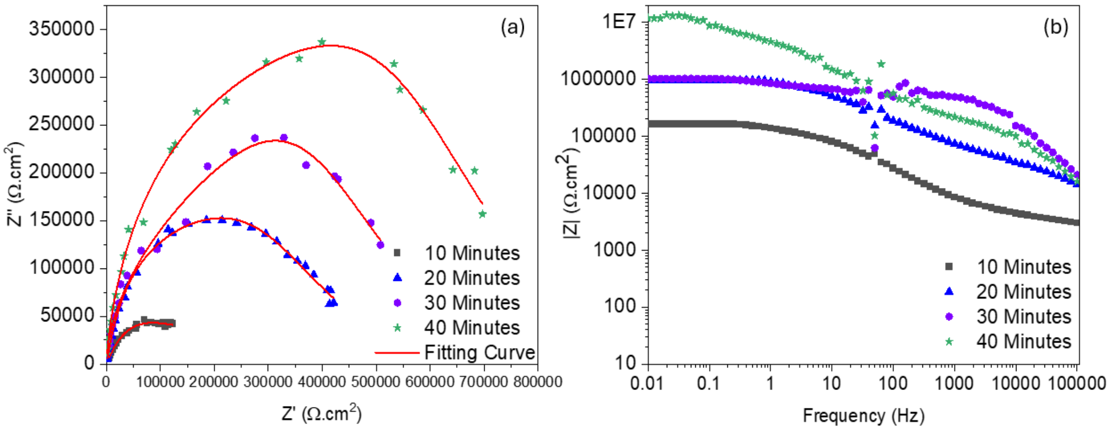

**Figure 14:** EIS of Alumina Blasted Samples at 1000 kPa Blasting Pressure with Different Anodization Time in SBF (a) Nyquist Plot (b) Bode-Impedance Modulus Plot

Likewise, the highest corrosion resistance for the A1000-AT40 sample is confirmed by the Bode-impedance modulus plot, shown in Fig. 14(b) at lower frequencies, with a value of 11840000 Ω.cm$^2$. The circuit parameter fitted values for A1000-AT10 – A1000-AT40 samples are provided in Table 8. The higher values of $R_f$ (45.5 kΩ.cm$^2$) and $R_{ct}$ (67.4 kΩ.cm$^2$) for the A1000-AT40 sample, in comparison to other anodized samples, provide confirmation of the protective characteristics of the barrier layer. $CPE_{dl}$ and $CPE_f$ tend to decrease as the anodizing duration increases, which means that the electrolyte is exposed to less of the film, leading to a more compact and pore-free anodized film.

The EIS data indicates that high values of surface oxide film resistance and charge transfer resistance of the samples blasted at 1000 kPa at 40 minutes of anodization time suggest that a protective anodized layer developed on alumina-blasted samples may be suitable for biomedical applications [20].

## Conclusion:

The findings of this study aid in developing biocompatible coatings on magnesium alloys for bone fixation implants. The results of potentiodynamic polarization scans of the pristine, quartz and alumina blasted samples at different blasting pressures revealed that blasting pressure and blasting media has significant role towards the development of anodized layer along with processing time. The surface blasted with alumina particles shows the development of anodized layer with better corrosion rate and polarization resistance. The increase in processing time results in better anodic film with full coverage. Similarly, the EIS data confirms the capacitance nature of the compact and pore free inner layer with porous outer layer on the samples blasted at 1000 kPa at 40 minutes of anodization time. The anodized layer develops on alumina blasted samples are superior than that of quartz blasted samples.

## References:

[1] X. Liu *et al.*, “Biofunctionalized Anti-Corrosive Silane Coatings for Magnesium Alloys,” *Acta Biomater.*, vol. 9, pp. 8671–8677, Nov. 2013.

[2] A. Zaffora *et al.*, “Tuning of the Mg Alloy AZ31 Anodizing Process for Biodegradable Implants,” *ACS Appl. Mater. Interfaces.*, vol. 13, pp. 12866–12876, Mar. 2021.

[3] H. Hermawan, D. Dubé, and D. Mantovani, “Developments in metallic biodegradable stents,” *Acta Biomater.*, vol. 6, pp. 1693–1697, May 2010.

[4] F. Witte, “The history of biodegradable magnesium implants: A review,” *Acta Biomater.*, vol. 6, pp. 1680–1692, May 2010.

[5] M. P. Staiger, A. M. Pietak, J. Huadmai, and G. Dias, “Magnesium and Its Alloys as Orthopedic Biomaterials: A Review,” *Biomater.*, vol. 27, pp. 1728–1734, Mar. 2006.

[6] H. Hornberger, S. Virtanen, and A. R. Boccaccini, “Biomedical Coatings on Magnesium Alloys—A Review,” *Acta Biomater.*, vol. 8, pp. 2442–2455, Jul. 2012.

[7] L. Zhao, C. Cui, Q. Wand, and S. Bu, “Growth Characteristics and Corrosion Resistance of Micro-Arc Oxidation Coating on Pure Magnesium for Biomedical Applications,” *Corros. Sci.*, vol. 52, pp. 2228–2234, Jul. 2010.

[8] M. Esmaily *et al.*, “Fundamentals and Advances in Magnesium Alloy Corrosion,” *Prog. Mater. Sci.*, vol. 89, pp. 92–193, Aug. 2017.

[9] S. Pan *et al.*, “Optimization of AZ31B Magnesium Alloy Anodizing Process in NaOH–$Na_2SiO_3$–$Na_2B_4O_7$ Environmental-Friendly Electrolyte,” *Coatings*, vol. 12, p. 578, Apr. 2022.

[10] J. T. D. de Oliveira *et al.*, “Sealing of Anodized AZ31B Magnesium Alloy in Lanthanum-Based Solution: Interplay Between Sealing Parameters, Surface Chemistry, and Corrosion Resistance,” *J. Mater. Eng. Perform.*, vol. 33, pp. 8156–8164, Jul. 2023.

[11] E. Merino, A. Durán, and Y. Castro, “Integrated corrosion-resistant system for AZ31B Mg alloy via plasma electrolytic oxidation (PEO) and sol–gel processes,” *Int. J. Appl. Glass Sci.*, vol. 12, pp. 519–530, Oct. 2021.

[12] L. A. de Oliveira, S. L. dos Santos, V. A. de Oliveira, and R. A. Antunes, “Influence of Anodization on the Fatigue and Corrosion–Fatigue Behaviors of the AZ31B Magnesium Alloy,” *Metals*, vol. 11, p. 1573, Oct. 2021.

[13] Y. C. Guan, W. Zhou, and H. Y. Zheng, “Effect of laser surface melting on corrosion behaviour of AZ91D Mg alloy in simulated-modified body fluid,” *J. Appl. Electrochem.*, vol. 39, pp. 1457–1464, Feb. 2009.

[14] W. Zhou, T. Shen, and N. N. Aung, “Effect of heat

treatment on corrosion behaviour of magnesium alloy AZ91D in simulated body fluid," *Corros. Sci.*, vol. 52, pp. 1035–1041, Mar. 2010.

[15] N. Afsharimani *et al.*, "Improving corrosion protection of Mg alloys (AZ31B) using graphene-based hybrid coatings," *Coatings*, vol. 13, pp. 143–150, Jan. 2022.

[16] A. Yabuki and M. Sakai, "Anodic films formed on Mg in organic, silicate containing electrolytes," *Corros. Sci.*, vol. 51, pp. 793–798, Apr. 2009.

[17] W. Ximei, Z. Ligun, L. Huicong, and L. Weiping, "Influence of surface pretreatment on anodizing film of Mg alloy and mechanism of the ultrasound during pretreatment," *Surf. Coat. Technol.*, vol. 202, pp. 4210–4217, May 2008.

[18] R. F. Zhang, D. Y. Shan, R. S. Chen, and E. H. Han, "Effects of electric parameters of anodic coatings formed on magnesium alloys," *Mater. Chem. Phys.*, vol. 107, pp. 356–363, Feb. 2008.

[19] F. Hussain, M. U. Manzoor, M. Kamran, and M. T. Z. Butt, "The effect of grit blasting on surface roughness and hardness of magnesium alloy AZ31B: A statistical study," *Phys. Met. Metallogr.*, vol. 124, pp. 1620–1631, Dec. 2023.

[20] L. A. de Oliveira, R. M. P. da Silva, A. C. D. Rodas, R. M. Souto, and R. A. Antunes, "Surface chemistry, film morphology, local electrochemical behavior and cytotoxic response of anodized AZ31B magnesium alloy," *J. Mater. Res. Technol.*, vol. 9, pp. 14754–14770, Dec. 2020.

[21] F. Hussain *et al.*, "Optimizing biocompatibility of Mg-AZ31B alloy through varied surface roughness and anodization time," *Iran. J. Mater. Sci. Eng.*, vol. 21, pp. 1–15, Sep. 2024.

[22] K. Saranya, S. Bhuvaneswari, S. Chatterjee, and N. Rajendran, "Titanate incorporated anodized coating on magnesium alloy for corrosion protection, antibacterial responses and osteogenic enhancement," *J. Magnes. Alloy.*, vol. 10, pp. 1109–1123, Apr. 2022.

[23] I. Johnson, J. Lin, and H. Liu, "Surface Modification and Coatings for Controlling the Degradation and Bioactivity of Magnesium Alloys for Medical Applications," in *Orthopedic Biomaterials*, B. Li and T. Webster, Eds. Cham: Springer, 2017.

[24] T. Sridhar, U. K. Mudali, and M. Subbaiyan, "Preparation and characterization of electrophoretically deposited hydroxyapatite coatings on type 316L stainless steel," *Corros. Sci.*, vol. 45, pp. 237–252, Feb. 2003.

[25] B. L. Luan, D. Yang, X. Y. Liu, and G. L. Song, "Corrosion protection of magnesium (Mg) alloys using conversion and electrophoretic coatings," in *Corrosion of Magnesium Alloy*, vol. 2, pp. 541–564, 2011.

[26] X. Cui *et al.*, "Corrosion behaviors in physiological solution of cerium conversion coatings on AZ31 magnesium alloy," *Appl. Surf. Sci.*, vol. 257, pp. 9703–9709, Sep. 2011.

[27] J. S. Li and J. Q. Liu, "Structure and Properties of Anodized Films Formed on AZ91D Magnesium Alloy," *Appl. Mech. Mater.*, vol. 66–68, pp. 1586–1591, Jul. 2011.

[28] E. Merino, A. Durán, and Y. Castro, "Integrated corrosion-resistant system for AZ31B Mg alloy via plasma electrolytic oxidation (PEO) and sol–gel processes," *Int. J. Appl. Glass Sci.*, vol. 12, pp. 519–530, Oct. 2021.

[29] E. O. Ningrum *et al.*, "Surface Coating Effect on Corrosion Resistance of Titanium Alloy Bone Implants by Anodizing Method," *Int. J. Technol.*, vol. 14, pp. 749–760, Jun. 2023.

[30] Z. U. Rahman, L. Pompa, and W. Haider, "Electrochemical characterization and in-vitro bio-assessment of AZ31B and AZ91E alloys as biodegradable implant materials," *J. Mater. Sci: Mater. Med.*, vol. 26, Jul. 2015.

[31] B. M. Fernandez-Perez, J. A. Gonzalez-Guzman, S. Gonzalez, and R. M. Souto, "EIS investigation of the corrosion resistance of a waterborne acrylic coating containing active electrochemical pigments for the protection of carbon steel," *Int. J. Electrochem. Sci.*, vol. 9, pp. 2067–2079, Apr. 2014.

[32] W. C. Say, C. C. Chen, and S. J. Hsieh, "Electrochemical characterization of non-chromate surface treatments on AZ80 magnesium," *Mater. Charact.*, vol. 59, pp. 1400–1406, Oct. 2008.

[33] M. Babaei, C. Dehghanian, and M. Vanaki, "Effect of additive on electrochemical corrosion properties of plasma electrolytic oxidation

coatings formed on CP Ti under different processing frequency," *Appl. Surf. Sci.*, vol. 357A, pp. 712–720, Dec. 2015.

[34] L. Zhang *et al.*, "Study on the anodic film formation process of AZ91D Mg alloy," *Electrochim. Acta*, vol. 52, pp. 5325–5333, May 2007.

[35] I. G. Ogunsanya and C. M. Hansson, "The semiconductor properties of passive films and corrosion behavior of stainless steel reinforcing bars in simulated concrete pore solution," *Mater.*, vol. 6, p. 100321, Jun. 2019.

[36] M. Santamaria, G. Tranchida, and F. Di Franco, "Corrosion resistance of passive films on different stainless steel grades in food and beverage industry," *Corros. Sci.*, vol. 173, p. 108778, Aug. 2020